Sub-micron weak phase particle characterization using the reconstructed volume intensities from in-line digital holography microscopy

Andres Barrio-Zhang[1] **and Arezoo M Ardekani**[1,*]

[1]School of Mechanical Engineering, Purdue University, West Lafayette, Indiana
[*]e-mail: ardekani@purdue.edu

ABSTRACT

Digital holography microscopy is a powerful technique for retrieving particle properties that are often challenging to obtain with other methods. However, analyzing holographic data using non-linear fitting algorithms and machine learning is difficult without prior information. In this paper, we present a novel technique for sizing and determining the refractive index of sub-micron, weak phase, spherical particles using the Rayleigh-Sommerfeld diffraction theory. Our method involves reconstructing the volume of synthetic holograms using the HoloPy software for particles of different sizes and material properties. We then fit a Gaussian function at the point of numerical re-focus, as given by the first local minima after the Gouy-phase shift, for size and sub-pixel position estimates. By retrieving the magnitude and location of the maximum scattered intensity, we build a scattered interpolant that relates all the parameters of interest. We demonstrate that our technique had a mean error in particle refractive index of 1.24 $\pm$ 1.74% with synthetic data and accurately estimates the size and refractive index of similar-sized nanoparticles in experiments. Compared to least-squares fitting, our method performs similarly with synthetic data but outperformed it with experimental data, showcasing its superior accuracy and reliability. Furthermore, we use our technique combined with function-fitting approaches. This hybrid method uses our proposed technique to approximate the initial conditions of non-linear fitting algorithms, leading to improved accuracy. Finally, we explore the potential of using the intensity cubes as well-defined thresholds to differentiate particles from interference caustics in a reconstructed volume. Overall, our results demonstrate the efficacy and accuracy of our technique for retrieving particle properties from holographic data, even when prior information was not available. This technique could have broad applications in the field of nanoparticle characterization.

Highlights

- The numerically reconstructed scattered intensity field from digital holograms is applied for size and refractive index measurements of nanoparticles.
- A scattered interpolant function is built using an intensity cube calibrated from synthetic hologram data sets.
- This technique is validated with synthetic and experimental data, and compared with least-squares fitting.

1 Introduction

Holography, a light interferometry technique first introduced by Gabor in 1949[1], has emerged as a powerful tool for the three-dimensional (3D) characterization of objects within the light path of a light source. Holograms offer a unique means of measuring a wide range of object properties, including size, position, and refractive index, by capturing the interference patterns generated by the reference and scattered light of the object of interest[2,3]. With advances in computational image processing and numerical reconstruction, digital holography microscopy (DHM) has become a highly versatile and non-invasive method for extracting a wealth of information from microscopic samples[4–6].

DHM has found numerous applications in the life sciences, where it has proven highly effective in tracking the motion of bacteria, microorganisms, and biological particulates across various length scales[7–10]. Furthermore, DHM has enabled accurate and high-throughput characterization of biological suspensions using tomographic flow cytometry[11–13]. Beyond the life sciences, DHM has also been successfully applied to the measurement of 3D flow fields in micro-channels by tracking the motion of particle tracers[14–17].

The use of digital in-line holography for tomographic imaging offers a distinct advantage over other methods in that a wealth of sample properties can be encoded into a single image, while the experimental setup is comparably simple and easily integrated with other microscopy instruments. A range of approaches have been proposed to solve for the inverse problem

of parameter estimation given a holographic image. One widely used method is non-linear Lorenz-Mie fitting, which can accurately determine particle size, location, shape, and refractive index[15,18–21]. However, this approach can be computationally demanding for concentrated, poly-disperse, and unknown-shaped particle samples, since it depends on accurately estimating the initial parameters of the analytical models used to describe the scattering object. To address these challenges, researchers have turned to Bayesian parameter estimations[22] and machine learning techniques that greatly accelerate fitting algorithms for complex samples[23–26]. Nonetheless, Monte-Carlo adds a layer of computational expense to an already computationally demanding task, and machine learning models rely on high-quality training databases, which can be difficult to construct for unknown samples and require considerable storage[26].

To overcome these limitations, a recent review has proposed combining non-linear fitting with machine learning-based initialization[27]. This hybrid approach uses machine learning algorithms to coarsely approximate the initial conditions of non-linear fitting algorithms, enabling accurate particle characterization while reducing computational complexity. While this approach holds great promise, it is essential to ensure the quality of the training database for machine learning models, particularly for unknown samples.

As a general and simpler alternative, volume reconstruction is a powerful technique that can provide qualitative and quantitative 3D approximations of a sample without the need for complex fitting algorithms or probabilistic parameter estimation. The key to this technique is the Huygens-Fresnel principle, which allows for the 3D electromagnetic field to be reconstructed through back-propagation. Each pixel in the 2D holographic image is taken as a source of a spherical wave, and convolution is performed with the original image, resulting in a 3D reconstruction of the sample.[28–30] The resulting image can be analyzed to identify the position and size of particles, as well as other important information such as material properties and concentration, even for non-spherical particles.[31]

While this technique is highly effective, it still faces challenges from human intervention and manual tuning. One such challenge is identifying the threshold that allows for accurate particle quantification. When the sample concentration is not known *a priori*, this becomes even more challenging. For example, Shangraw et al.[5] developed a threshold algorithm that matches the threshold value to the known concentration iteratively. However, such algorithms can be computationally expensive, requiring significant tuning, and aren't applicable to unknown or polydisperse particle distributions. To address this need for more automated thresholding algorithms, Toloui and Hong[16,17] have developed complex signal-to-noise ratio enhancement and segmentation algorithms. These algorithms can effectively extract information such as concentration and size. However, they are computationally complex, and, through the many voxel manipulations, discard important optical information about the particles present in the reconstructed volume.

Thus, there is a critical need for a simple, accurate, and generalizable technique that can extract particle information such as the size and refractive index. Such a technique would greatly enhance the capabilities of volume reconstruction and open up new possibilities for applications in a variety of fields.

Recently, Romanov et al. have demonstrated that using the main peak of the amplitude spectrum of light scattering patterns can result in information about the particle size and refractive index.[32] Similarly, in this work, the in-line DHM reconstructed amplitude is used to provide size and refractive index measurements for samples containing spherically shaped nanoparticles (NP). This is achieved by creating and calibrating an intensity threshold data cube, built with synthetic holograms typically used for non-linear fitting. The intensity of the object scattered field, with and without the reference field, yield size iso-surfaces and can thus be used as scattered linear interpolants for parameter estimation. Reconstructing the 3D volume through back-propagation with a Rayleigh-Sommerfeld convolution kernel results in points of maximal intensity for both synthetic and experimental data, which can then be used as inputs for the scattered interpolant function to solve the inverse problem. As opposed to other propagation methods for particle parameter estimation, our technique can solve for the particle size and refractive index simultaneously, with similar accuracy to non-linear fitting regimes, however, having a faster computational time (500x faster) and more robust analysis method when initial parameters of the samples are unknown. We compare the performance of this algorithm with synthetic and experimental data to non-linear least squares fitting using the Levenberg-Marquadt algorithm. We find that with synthetic data, close initial parameter initialization of the least squares fitting regime results in more accurate results; however, having a 30% initial parameter estimation can have an erroneous converged solution due to gradient descent, with up to 80% error, even with synthetic data devoid of noise. Finally, we propose a hybrid approach that combines our technique as a coarse initial parameter estimation with least squares fitting for refinement. This eliminates the need for machine learning and introduces a robust analysis method for holographic particle image analysis. Our technique provides an accurate, efficient, and non-invasive method for the measurement of particle size and refractive index, which has the potential to impact a wide range of fields including materials science, biotechnology, and environmental monitoring.

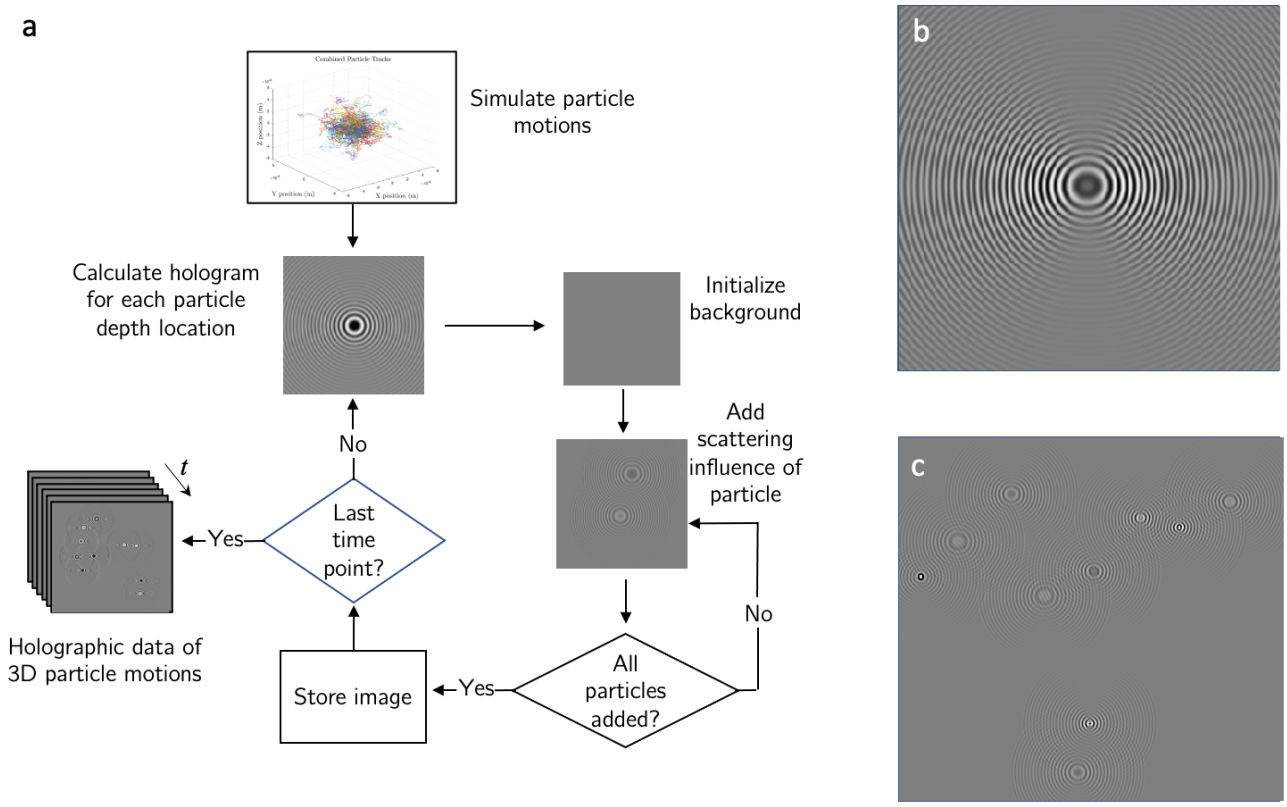

Figure 1. a) Flow chart for synthetic data generation used in this study. b) Single 500nm NP scattering pattern at a 2μm distance from the imaging plane, calculated using HoloPy. c) Example of multiple synthetic NP holograms superposed in an image.

2 Materials and Methods

2.1 Synthetic Data Generation

Synthetic holograms of spherical NPs were built using the HoloPy python library[33]. This code package has been shown to provide accurate estimations of experimental holograms by taking into consideration the multiple parameters affecting the image formation, such as aberrations from the imaging lens.[34] Fig.1 shows a flow chart of the synthetic data generation algorithm to create images of particle suspensions. The particle's position in three dimensions was modeled by imposing external disturbances governing their motion, such as a flow field for Brownian motion. To obtain holographic images of the particles at different depths, we calculated the corresponding holographic patterns for each particle. We added them to their respective frames by superimposing the holographic pattern onto a uniform background. Particle suspensions of different sizes and optical materials were modeled. For each hologram simulated, the parameters matched the experimental conditions, such as illumination from a laser light with wavelength $\lambda = 632.8$nm, linear polarization, a medium refractive index of $n_m = 1.33$, and magnified pixel dimension of 100nm/pixel.

2.2 Particle Characterization

A holographic image is a result of the reference wave interacting with the object scattered wave and can be expressed with the intensity of these fields by the following[5]

$$I_H(x,y) = |R+O|^2 = |R|^2 + |O|^2 + RO^* + R^*O, \tag{1}$$

where x and y are the in-plane coordinates within the image, taken from the image center, R and O represent the complex wave values of the reference wave and object wave, respectively, at the focus plane of the imaging system, and * denotes the complex conjugate. All hologram intensities were normalized by the reference field, yielding the normalized hologram images as follows

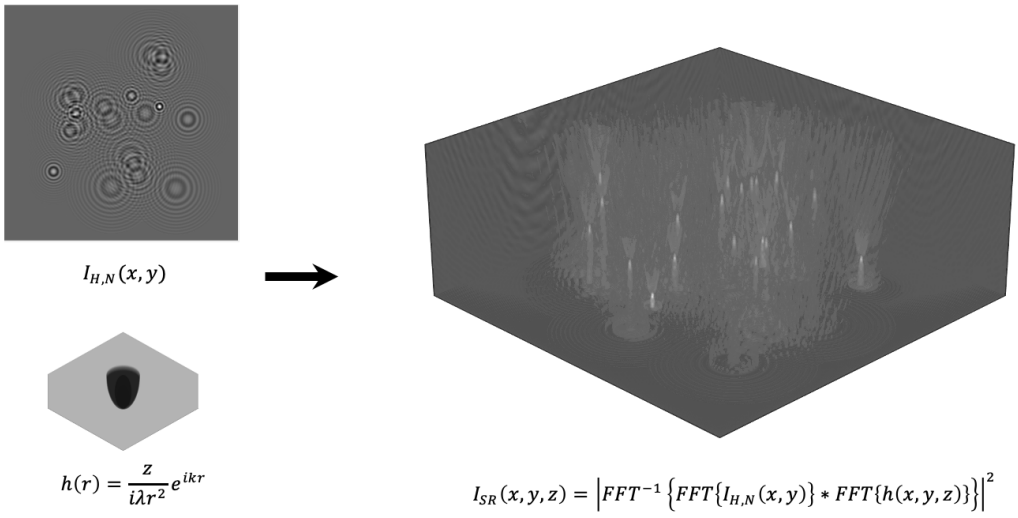

Figure 2. Rayleigh-Sommerfeld propagation applied to a holographic image. The holographic pattern pixel intensity converges at the particle position in 3D space.

$$I_{H,N}(x,y) = \frac{1}{|R|^2}(|R|^2 + |O|^2 + RO^* + R^*O) = 1 + \frac{|O|^2}{|R|^2} + \frac{RO^* + R^*O}{|R|^2}. \tag{2}$$

We used normalized holograms for all of the algorithmic analyses present in this paper.

The reconstructed volume was calculated with a convolution of the normalized hologram image with the Rayleigh-Sommerfeld diffraction kernel[35], given by

$$I_{SR}(x,y,z) = |I_{H,N}(x,y) \circledast h(x,y,z)|^2, \tag{3}$$

$$h(z,r) = \frac{z}{i\lambda r^2} e^{ikr}, \tag{4}$$

where I_{SR} is the reconstructed volume of the normalized hologram with the reference and object wave, z is the axial direction, λ is the wavelength of light, $k = \frac{2\pi n}{\lambda}$ is the wavenumber, and $r = \sqrt{x^2 + y^2 + z^2}$ is the radial coordinate. The reconstructed volume was reconstructed for the scattered field only by subtracting the reference wave, given by 1 for the normalized holograms

$$I_S(x,y,z) = |(I_{H,N}(x,y) - 1) \circledast h(x,y,z)|^2. \tag{5}$$

The propagation kernel voxels were first constructed for the volume analyzed, then 2D convolution was performed iteratively for every z-plane. To speed up the computation, the convolution was solved using Fourier convolution theory, given by

$$I_{SR}(x,y,z_i) = |FFT^{-1}\{FFT\{I_{H,N}(x,y)\} * FFT\{h(x,y,z_i)\}\}|^2, \tag{6}$$

where FFT is the 2D Fast Fourier Transform in the x-y plane, z_i is the location in the z-axis, and $*$ denotes the point-wise multiplication in the Fourier space. To reduce aperture diffraction and spectral leakage effects from the reconstruction process, the reconstructed volume for I_{SR} was point-wise divided by a reconstructed volume from an image of the same size filled with ones (Fig. S1). Fig. 2 shows an example of a reconstructed I_{SR} volume for a synthetic image of an NP suspension.

The four-parameter data cube was constructed by extracting the maximum voxel intensity of the scattered field for each particle size and refractive index, ranging from 200-950nm in diameter and 1.4-1.6 values of refractive index, respectively. A scattered interpolant was built using MATLAB, approximating the parameters of the particle through linear interpolation.

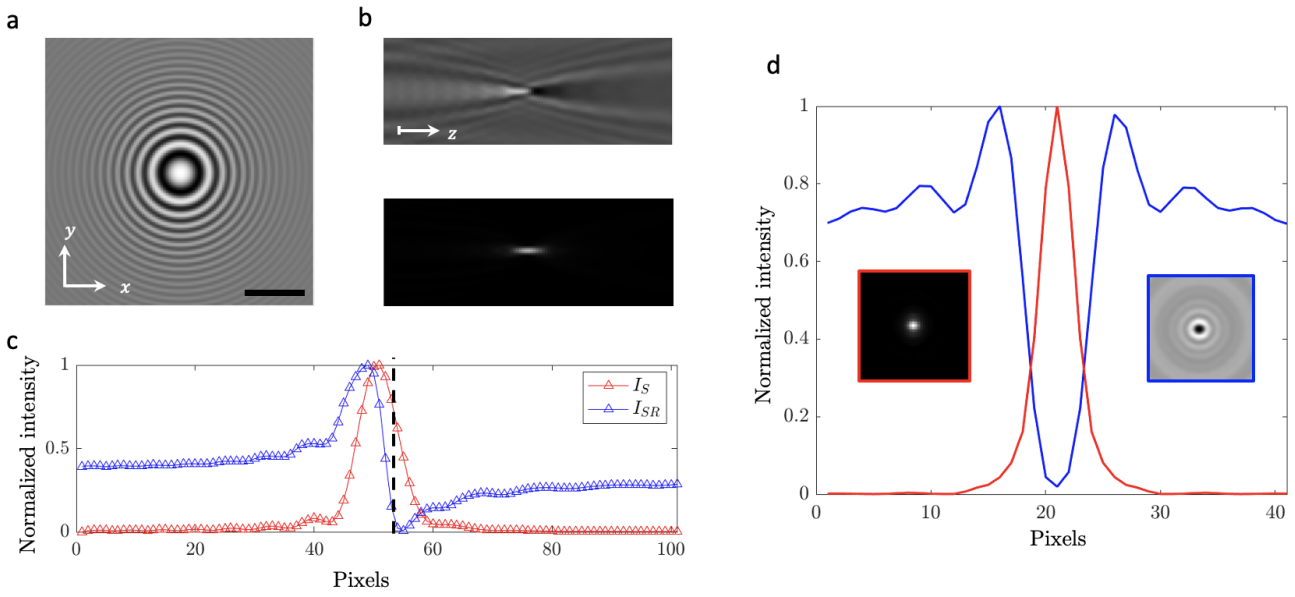

Figure 3. a) Normalized synthetic hologram of a 500nm particle at $5.5\mu m$ from the imaging plane, and its corresponding propagation of b) I_{SR} and I_S in the x-z plane. The scale bar is $5\mu m$. c) Axial intensity distributions at the particle center along the z direction. The dashed line indicates the actual particle location in the z-direction.
d) Normalized intensity at the center of the numerically refocused particle in the x-direction for I_{SR} (blue) and I_S (red). The pixel size is 100nm.

To solve for the refractive index of the particle, information about the particle's location and size had to be calculated by other methods. We explored the commonly used particle location and numerical re-focusing by the minimum in the reconstructed volume technique[36–38] but found that the particle location error and corresponding size error varied greatly depending on the refractive index. This is further explored in the work by Shangraw and Ling[5] where they found a relationship between the localization error and the acquired phase shift from the weak phase object. Instead, we found that by using the first local minima after the maximum in the I_{SR} reconstructed volume rather than the global minimum, we greatly reduced the refractive index dependence on the localization error and, consequently, the size estimation error. We tested different combinations from both reconstruction fields to determine the size and location of the particles (Fig. S2 and Fig. S3). We found that using the local minima in I_{SR} as the refocusing position and the corresponding intensity distribution of I_S as a measure for the particle size yielded the best results. We chose to fit a Gaussian function to estimate the particle size by twice the calculated standard deviation, however, other functions could potentially be used, such as a Voigt profile or Lorentzian distribution. This way, we reduced the manual threshold also present in maximum edge detection methods[37,39]. Fitting a Gaussian curve on the refracted field additionally allowed for sub-pixel particle localization and re-scaling of the corresponding intensities (Fig.3). Once the particle location and size were approximated, the parameter values of the particle scattered intensity, size, and location, were fed into the scattered interpolant function, and the refractive index was estimated.

2.3 Experiments

Samples were injected to micro-channel slides (ibidi µ-Slide VI 0.4) and pumped at different flow rates using a syringe pump (Chemyx Fusion 4000). The samples were imaged at 60X magnification using a Nikon TiE microscope. Images were acquired using a Zyla 5.5 sCMOS camera at 50ms exposure time. The holographic system was adapted from Molaie et al.[40]. Briefly, the holographic system consists of a 632.8nm wavelength laser (Melles Griot 05-LHR-151 HeNe Laser 15mW) passing through a linear polarizer (Thorlabs). The laser then passes through a 40X objective focusing on a pinhole as a means of spatial filtering. Finally, the laser light passes through a collimating lens and is redirected towards the sample and microscope optical train through a mirror. To reduce the effect of the twin image, we limited our analysis to particles located in $z > 0$ by focusing the image on the bottom of the microchannel. A diagram and picture of the holography setup are seen in Fig.4. Polystyrene (Spherotec) and silica (Millipore Sigma) NPs with a nominal diameter of 500nm were used for validation of the technique, as both have a similar size yet differ in optical properties.

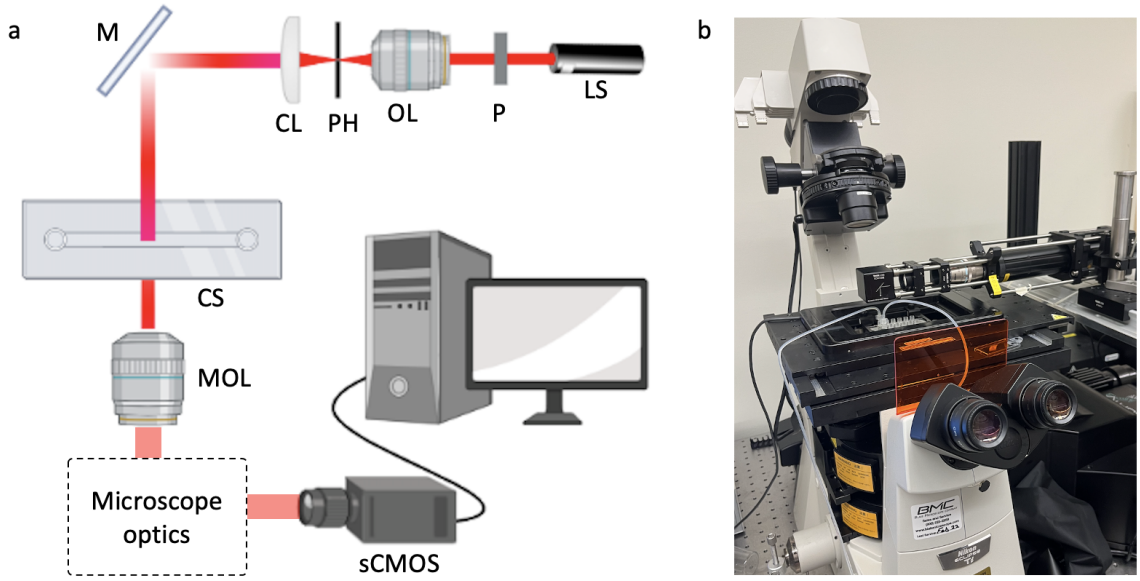

Figure 4. a) Experimental setup diagram. LS: Laser source, P: Linear polarizer, OL: Objective lens, PH: Pinhole, CL: Collimating lens, M: Mirror, CS: Channel slide, MOL: Microscope objective lens. b) Picture of the experimental setup.

2.4 Image Processing

The experimental images were processed by background normalization and subtraction. A similar approach to Molaei et al.[40] was taken to calculate the background using Correlation-based De-Noising (CDN). Fig. 5 showcases the algorithm and compares it to a commonly used approach of Mean Window De-Noising (MWDN). The mean-window background was calculated from 100 images. Small vibrations from the experimental setup show that the background calculated from MWDN is not sufficient to provide a high-quality normalized image. These vibrations caused the background caustic and speckle patterns to shift slightly throughout the data acquisition period, leading to the fluctuations seen in Fig. 5a. A representative background was calculated to normalize the image by setting a cutoff value to the cross-correlation coefficient, given by

$$CC(t_i,\tau) = \frac{\sum_m \sum_n (I_H(m,n;t_i) - \overline{I_H}(t_i))(I_H(m,n;t_i+\tau) - \overline{I_H}(t_i+\tau))}{\sqrt{(\sum_m \sum_n (I_H(m,n;t_i) - \overline{I_H}(t_i))^2)(\sum_m \sum_n (I_H(m,n;t_i+\tau) - \overline{I_H}(t_i+\tau))^2)}}, \tag{7}$$

where t_i is the time point of interest in the image set, τ is the time offset it is compared with, m and n indicate different pixel values and $\overline{I_H}$ denotes the average intensity of the image at the respective time points. The averaged reference field background and normalized hologram image are expressed as

$$I_{H,R}(x,y,t_i) = \frac{1}{N}\sum_{i=1}^{N} I_H(x,y;CC(t_i,\tau) > k), \tag{8}$$

$$I_{H,N}(x,y,t_i) = \frac{I_H(x,y,t_i)}{I_{H,R}(x,y,t_i)}. \tag{9}$$

Since the samples consisted of dilute concentrations, analyzing single-particle images, a cross-correlation coefficient value above $k = 0.95$ was found to provide the best quality images. Additionally, images around the time point of interest, given by a 10-image window, were disregarded to avoid contributions from self-referencing.

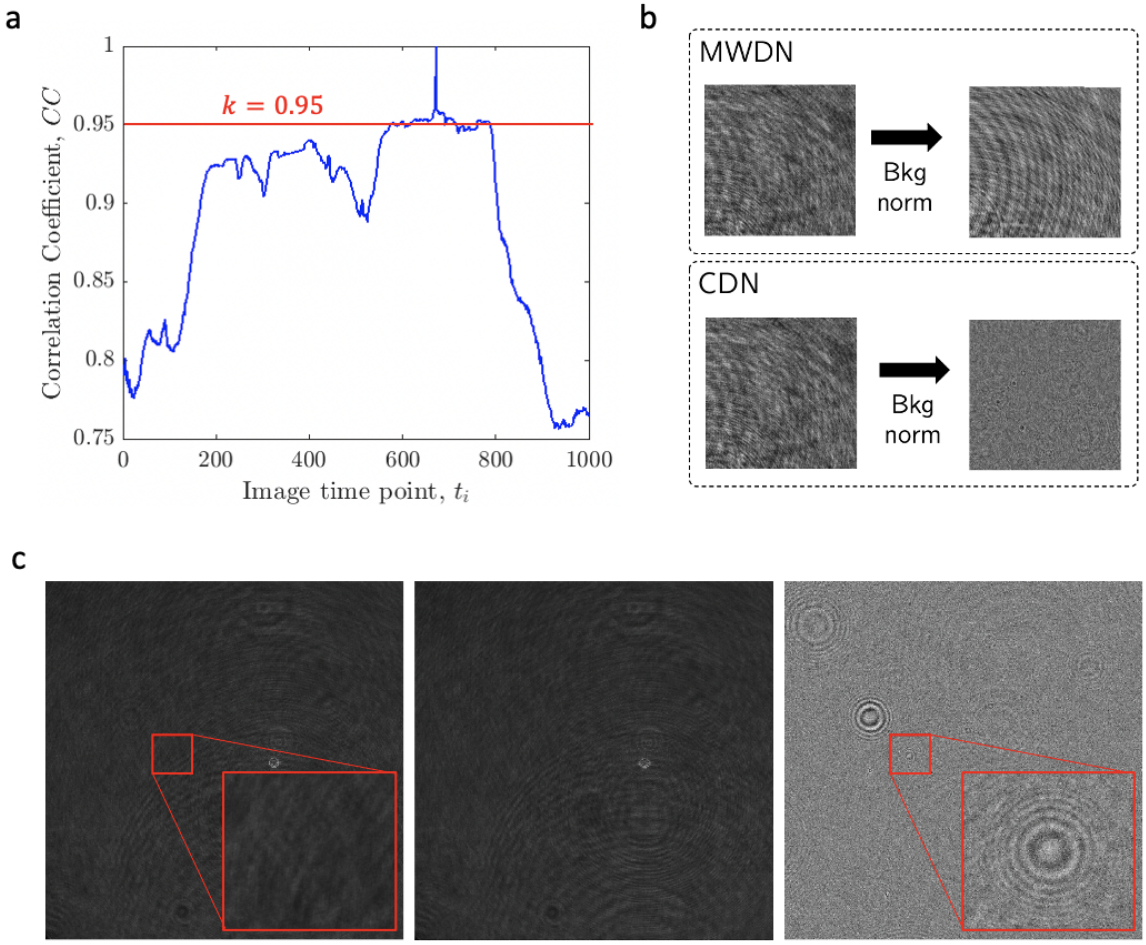

Figure 5. a) Cross-correlation coefficient calculation between image at the time point $t_i = 670$ and all other images in a data set. The fluctuations in this coefficient indicate vibrations within the setup. b) Comparison between MWDN and CDN, showcasing CDN's superior hologram normalization capability. c) Images of a raw hologram I_H with inset of 500nm polystyrene particle (left), the calculated averaged reference background $I_{H,R}$ (middle), and normalized hologram $I_{H,N}$ with inset clearly showing the contrast improvement.

3 Results

3.1 Depth, size, refractive index, and intensity correlation

Simulated holograms of different particle sizes and refractive indices centered on the image were used to determine the data cube for the intensity threshold. Each 201×201 pixel (0.1μm/pixel) hologram image corresponding to one particle size was simulated in axial steps of 100nm, for a total reconstruction volume of $20.1 \times 20.1 \times 10\mu$m with 4 million voxels. Fig. 6 shows the data acquisition for a single 500nm particle. The variation of the refractive index leads to a change in the maximum I_S peak intensity but doesn't change the peak location. However, a localization error was introduced, but this was mostly dependent on the size and not the refractive index. The maximum value for each particle reconstruction was retrieved as seen in Fig. 6a, where the axial intensity's maximum values correspond to the particle locations. A similar distribution is noticed by extracting these values for a variety of refractive indices, with a different relative intensity variation per depth.

Extending these principles to different particle sizes, the data cube for the intensity threshold of different particle sizes and refractive indices can be created. Fig. 7 shows these for both I_S and I_{SR}. This is a four-dimensional array containing information about the axial location, intensity, refractive index, and size. Each surface corresponds to a different particle size. The data cubes shown here are for sub-micron particles above the diffraction limit of the imaging system. Interestingly, for both data cubes created, iso-surfaces based on size are noticed, indicating that this can be used for parameter estimations by a scattered interpolant function given information on the other parameters.

3.2 Validation with synthetic data

Fig. 8a and Fig. 9a show the size estimation error when using the global minimum in the axial intensity distribution of I_{SR} at the particle center. The size estimation varied considerably when changing the refractive index of the particles, as the actual particle location within the reconstructed volume differs from the global minimum location. The global minimum location is created by the contrast inversion by the Gouy phase shift, which is dependent on the size and refractive index of the scatterer. This resulted in a large size estimation error, even for the same particle at the same axial location but with a different refractive index, represented by the shaded regions corresponding to the standard deviation of the error in the estimated size with respect to the refractive index. It was found that larger refractive indices will lead to different minima locations within the optical axis, thus, causing an erroneous refocusing metric. The refocusing position was confined to the first minima after contrast inversion, both the dependence on the refractive index, and corresponding size estimation, were improved. Fig. 8b and Fig. 9b show this, both significantly reducing the shaded regions, hence the refractive index dependence on the size measurement, as well as improving error estimation bounds.

It is important to note that for particles close to the pixel size, such as in the range of 200-350nm size estimation yielded a much larger error than in the other data sets, consistently overestimating the size. This can be improved by increasing the magnified pixel dimensions with a larger magnification and numerical aperture. For the remaining synthetic data comparisons with least squares fitting, we limited our analysis to particle sizes above 350nm.

Fig. 10 shows the refractive index estimation for particles at a depth of $5\mu m$, varying in size and RI as previously described. A single surface can be extracted from the data cube, where the scattered interpolant function is acting. With the previous size measurement estimation from the synthetic images, all parameters for inputs within the scattered interpolant can be used to estimate the refractive index. The maximum and minimum errors are $\pm 6\%$, with a mean of 1.24% and a standard deviation of 1.74%. This surpasses the capability of previously published RI estimation methods.

It was difficult to compare the non-linear least squares to this technique for the entire data set, considering the former heavily relies on the initial conditions for parameter estimation. To provide more information on how the Levenberg-Marquadt algorithm depends on the accuracy of the initial parameter estimation, each parameter was varied independently from the ground truth of a single particle. Fig. 11 shows the results. For refractive index measurements, underestimation of the refractive index yielded the largest converged solution error of -83% for an initial parameter error of 30%. Overestimation of the refractive index didn't produce significant differences in the converged solution error. Even when parameters were relatively close to the ground truth, all solutions overestimated the refractive index by 1.2%. Many of these trends are shared for the size estimation using this technique, however, here the largest error comes from initial particle coordinates x_p, y_p, and z_p. The particle coordinates can be estimated to an acceptable degree of accuracy, even using the built-in least squares fitting regime, by performing volume reconstruction. Additionally, a Radial Variance Transform (RVT) could be performed to estimate the particle coordinate without the need for volume reconstruction[41]. Overall, these plots served to convey the importance of accurate initial parameter estimation to reach an acceptable level of accuracy with least-square fitting algorithms.

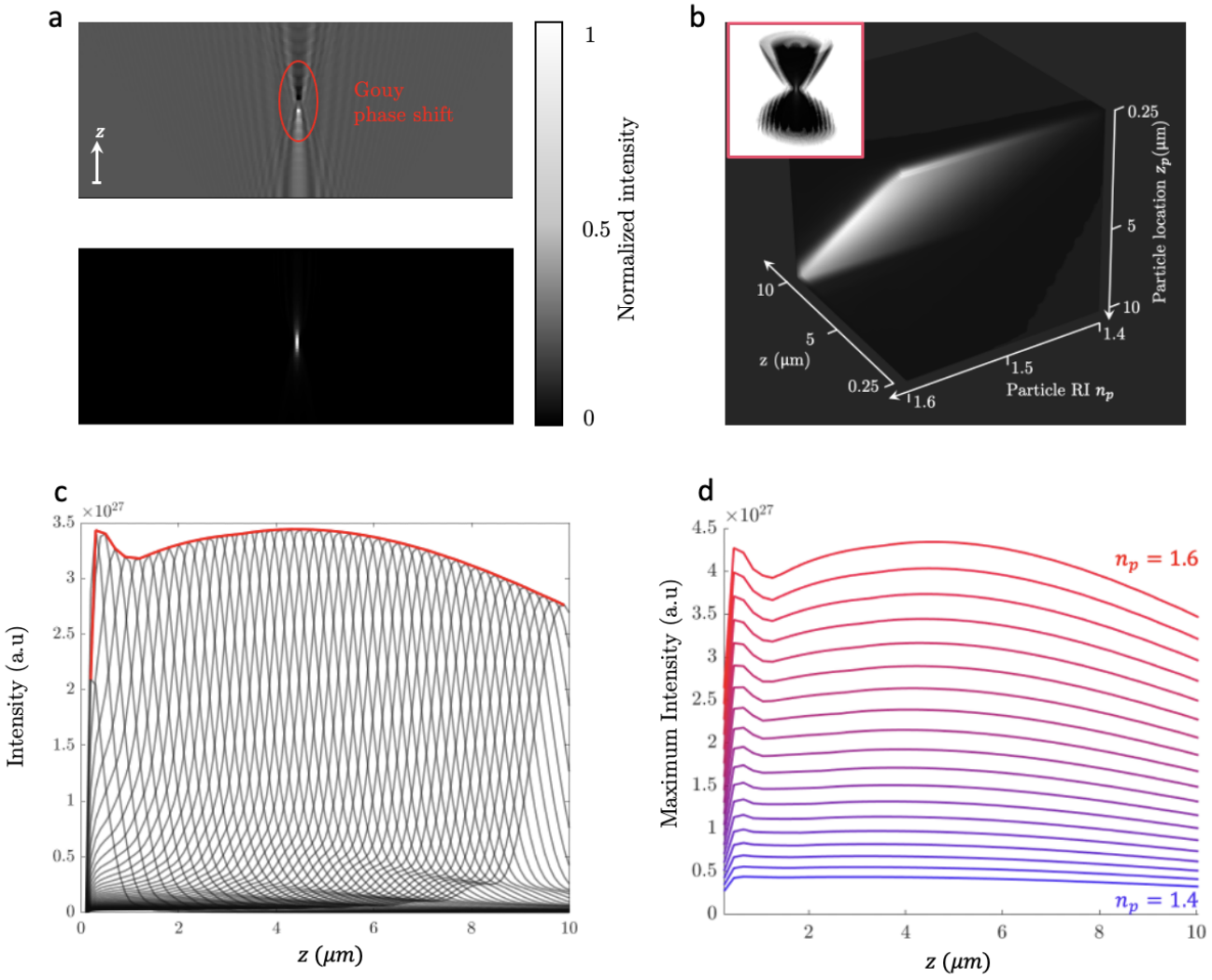

Figure 6. Depth intensity correlation and refractive index dependence. a) Normalized images in the xz-plane of the reconstructed volume for I_{SR} (top), showing a Gouy phase shift, and I_S, where the point of maximal intensity is recorded. b) Maximum intensity projection data cube for a single 500nm diameter synthetic particle. Each z-slice corresponds to a different axial location for the generated hologram. Inset shows a 3D intensity projection of a single hologram's reconstruction. c) Axial intensities for each hologram with $n_p = 1.56$. Gray lines are the axial intensities for each hologram depth. The red line is the maximum intensity of each axial distribution. d) Refractive index dependence on the maximum axial intensity for a 500nm particle. Each colored line corresponds to a different refractive index, evenly distributed from $n_p = 1.4 - 1.6$

.

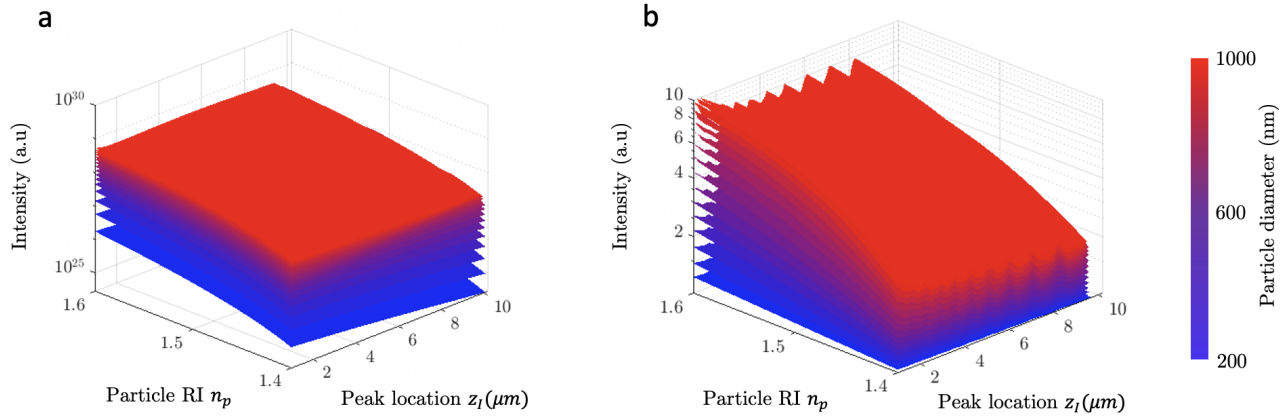

Figure 7. Data intensity threshold cube for different particle sizes and refractive indices at varying axial depths. a) Maximum peak intensities in I_S. b) Maximum peak intensities in I_{SR}. Each surface corresponds to a different particle size.

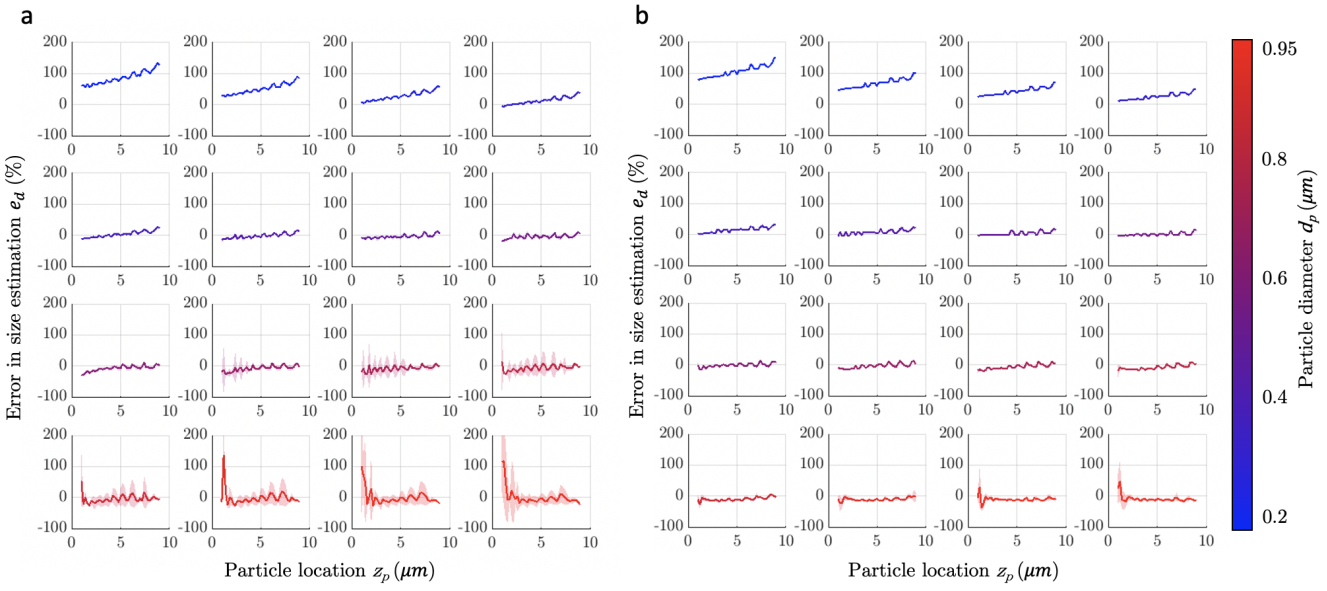

Figure 8. Mean percentage error in size measurements of different synthetically generated particles using the x-intensity. a) Size estimation error using global minimum b) Size estimation error using local minimum. The shaded regions represent the standard deviation of the error in the estimated size with respect to the refractive index, ranging from 1.4-1.6.

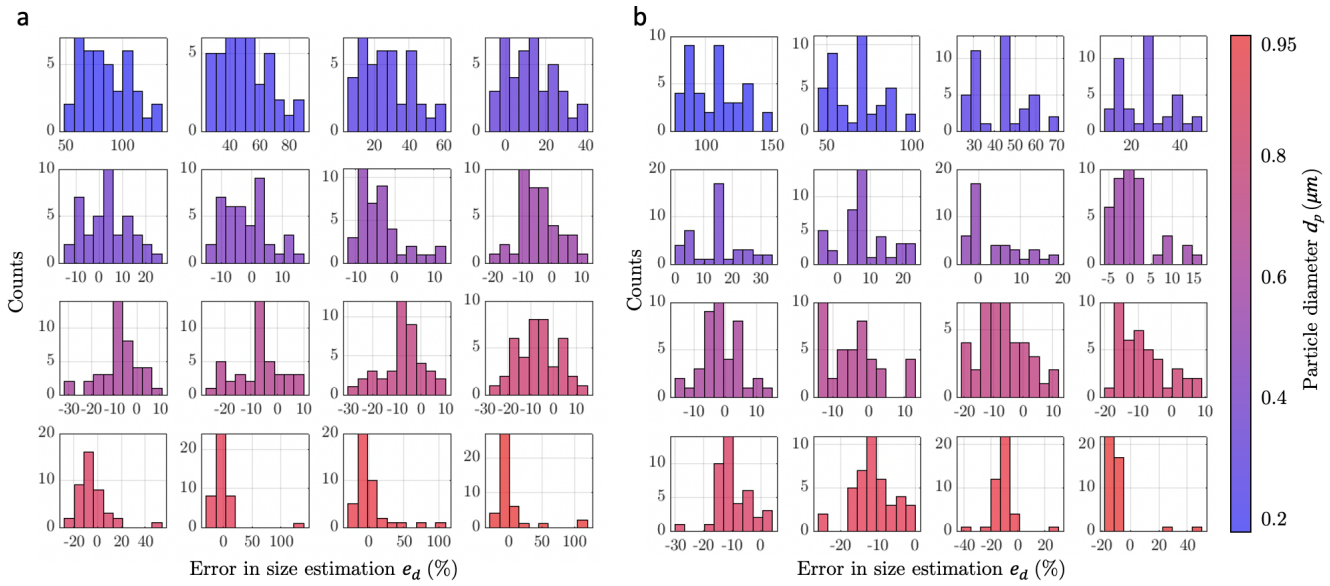

Figure 9. Histogram of errors in size measurements of different synthetically generated particles using the x-intensity. a) Size estimation error using global minimum b) Size estimation error using local minimum

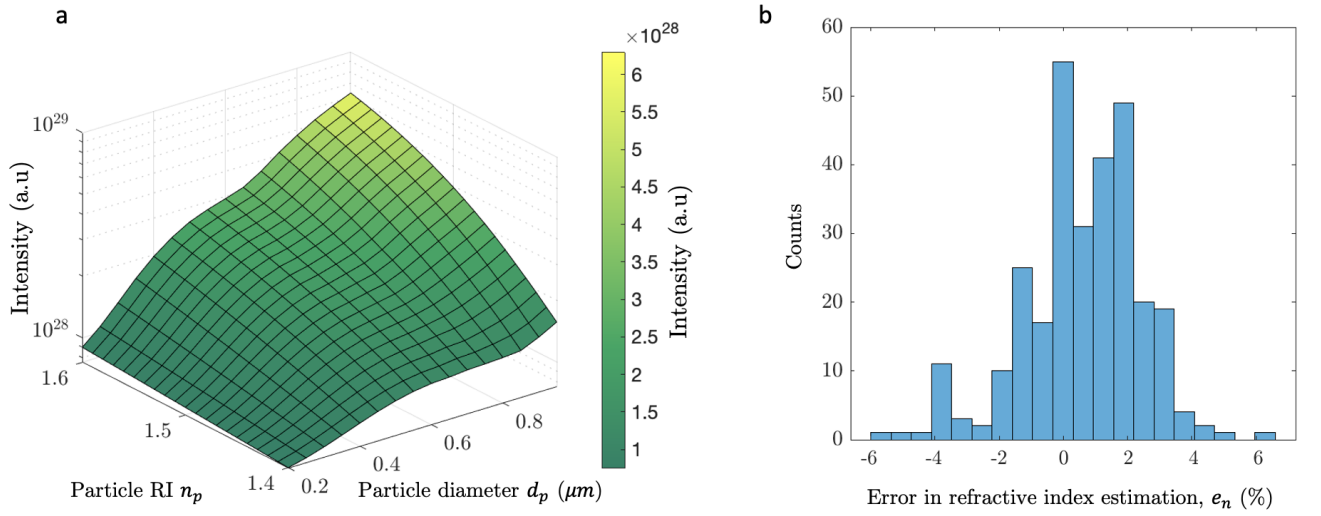

Figure 10. Measurements of RI for synthetic particles located 5μm from the imaging plane. a) Intensity surface relating RI, particle size, and intensity of I_S. b) Measured RI error using a scattered interpolant and the calibration surface.

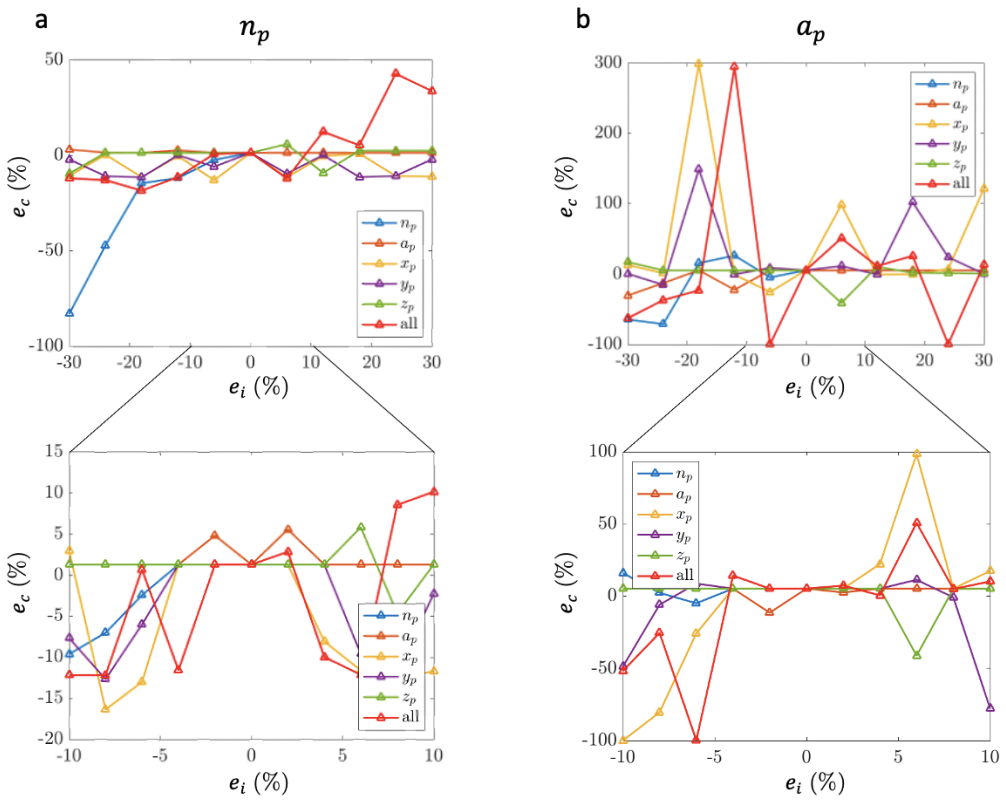

Figure 11. Converged solution error (e_c) for a particle with $n_p = 1.5$ and $a_p = 250nm$, with different errors in initial parameter estimation (e_i). a) Refractive index. b) Particle radius.

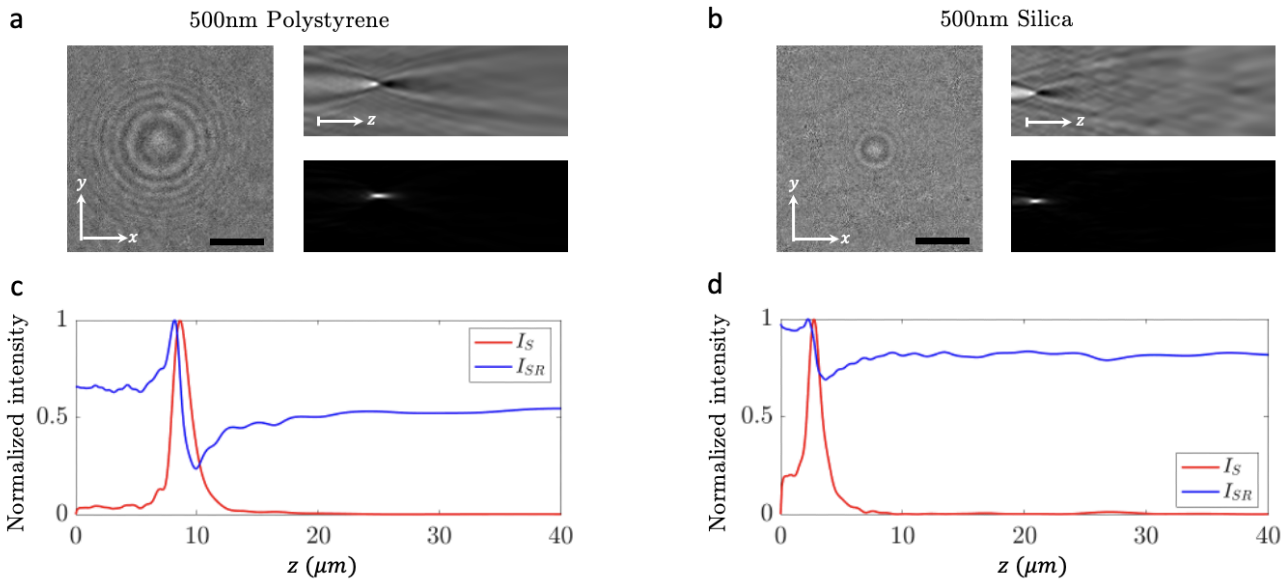

Figure 12. Experimental holograms for 500nm particles suspended in water (a,b), their reconstructed volumes I_{SR} (top) and I_S (bottom), and the corresponding normalized intensity plots at the particle center for the reconstructed volumes of each particle(c,d). The scale bar is $5\mu m$.

3.3 Experimental validation

Experimental images of NPs were acquired with the setup in Fig 4. NPs of similar size, but with different optical properties, were chosen to demonstrate the distinction in refractive index. The focal position of the microscope was adjusted to image the bottom of the channel slide, thus reducing the effect of virtual image generation in the reconstructed field. A dark image was taken and subtracted from the experimental images to eliminate effects from dark shot noise, as the laser power was reduced after passing through the linear polarizer and spatial filtering. Fig. 12 shows an example of the experimental hologram images and their reconstructed volumes. A new intensity calibration cube to use as a scattered interpolant was built for this experimental dataset, shown in Fig. 13b as many of the holograms resided past the limits of the previous intensity cube. Interestingly, the size iso-surface distinction was more apparent in the far-field scattered intensity, further conveying its usefulness as a scattered interpolant. Fig. 13a shows the results for size and refractive index estimations using our technique. The refractive index estimations (mean $\pm$ standard deviation) for silica and polystyrene were 1.4193 ± 0.0256 and 1.5712 ± 0.0363, respectively, which are within the bounds of previously reported values[42–44]. The measured size for silica and polystyrene particles were 409.33 ± 44.46nm and 471.70 ± 29.69nm. These are in agreement with the values reported by the manufacturer. The expected size ranges for the nanoparticles are 450-550nm nominal size with 10% error for silica (Millipore Sigma) and 400-600nm nominal size for polystyrene (Spherotech). We conducted Dynamic Light Scattering (DLS) size measurements with the Malvern Zetasizer nano ZS and have included a comparison in Fig. S4.

3.4 Hybrid method with least-squares fitting

To test the integration of the proposed technique with least-squares fitting, uniformly bounded random variables for initial parameter estimations were used to simulate the initialization of unknown parameters. The results were compared when the solutions were found from the scattered interpolant. The values for n_p, a_p, and the three-dimensional coordinates of the particle were bounded within reasonable estimates and matched those from the intensity calibration cube. As seen in Fig.13c, initializing the least squares algorithm led to a consistent underestimation of the refractive index and inaccuracy in the particle size estimation. Using the solutions from Fig. 13a, the calculated refractive index and particle size showed improvements, but were still largely inaccurate in comparison with the interpolant technique. The reasons for this large discrepancy were unexpected and further explored in the discussions section.

4 Discussion

The reconstructed volume already partially solves the inverse problem by approximating the electromagnetic field through the Helmholtz reciprocity and Huygens-Fresnel principles with the Rayliegh-Sommerfeld diffraction kernel. This is why the particle position and size can be measured, seen commonly with other methods. However, as it is demonstrated in this work,

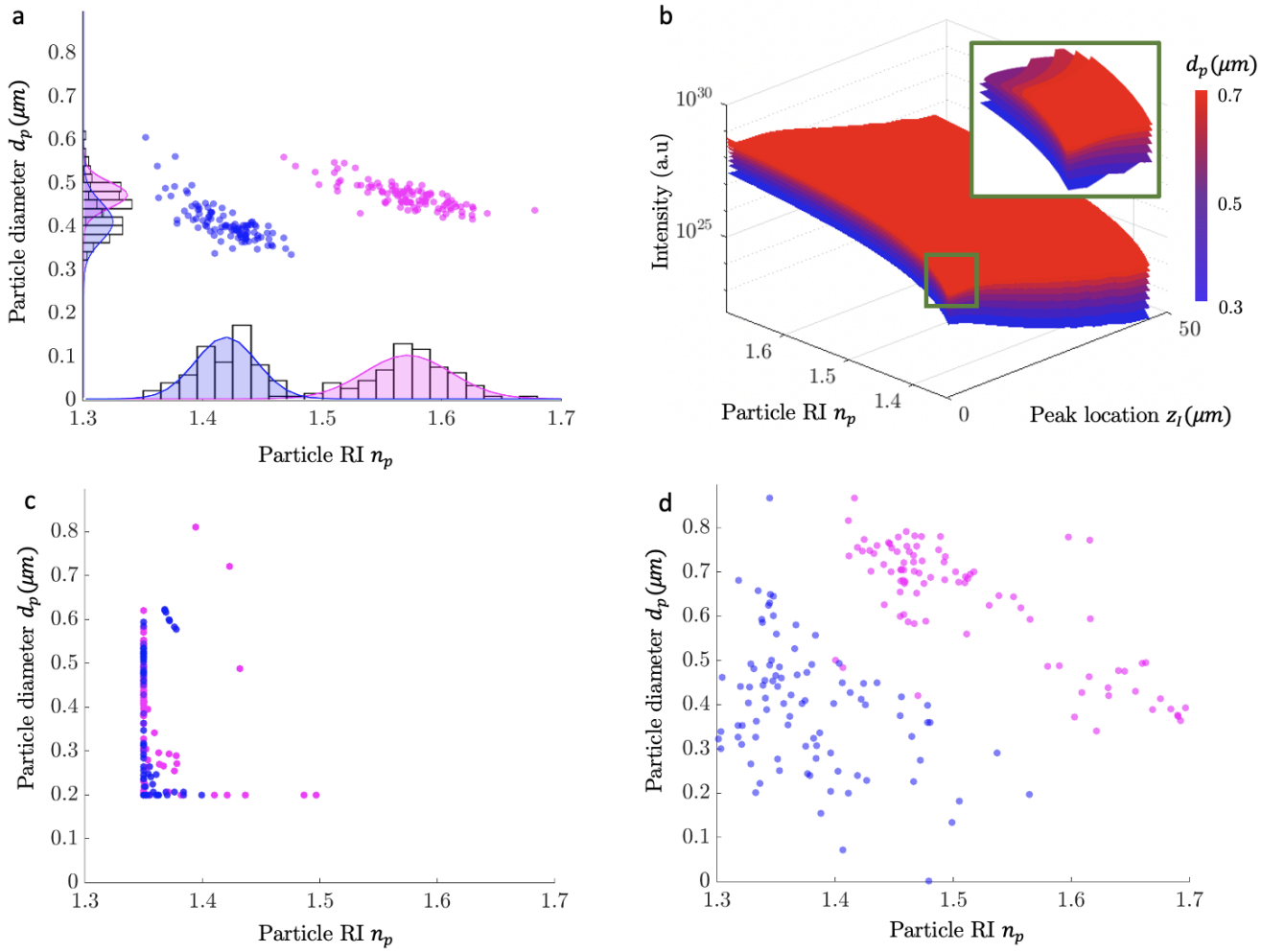

Figure 13. a) Scatter plot of calculated particle diameters and refractive indices for 200 holograms of 500nm polystyrene (magenta) and silica (blue) NPs. The histograms of each parameter are shown with Gaussian distributions. b) Intensity cube built with synthetic holograms used as a scattered interpolant with the experimental holograms. Inset shows the size iso-surface separation. c) Parameter initialization with uniform prior distributions, showing consistent underestimation and poor accuracy. d) Parameter initialization from solutions with the proposed technique.

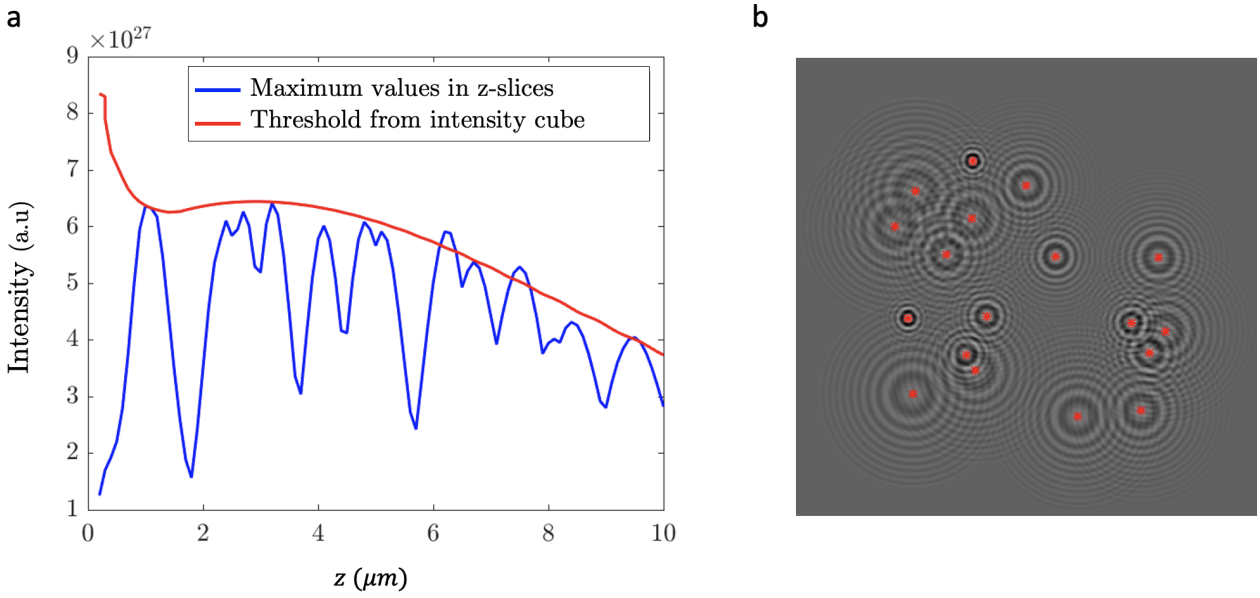

Figure 14. Employing the intensity cube as a threshold to differentiate the background from the particle holograms. a) Single I_S intensity line per depth (red) at the particle locations for $d_p = 500nm$ and $n_p = 1.56$ particles. The maximum intensity at each calculated z-location image from the reconstructed volume is recorded and shown to follow the trend of the threshold, where the peaks correspond to particle locations. b) Synthetic hologram with 18 particles. All particle locations (red markers) can be determined by using the threshold defined from the calibration intensity cube.

the reconstructed volume additionally encodes information about the particle's optical properties in the reconstructed intensity field, leading to unique distributions of intensities in particle size iso-surfaces. This idea can be extended to model different particle sizes and optical properties by reducing the number of fitting parameters, thus potentially improving fitting algorithms based on non-linear least squares fitting and machine learning.

After considerable improvements using CDN, the image pixel values still varied from each frame, leading to non-smooth intensity distributions. This affected the accuracy of the solutions when performing Levenberg-Marquadt least-squares fitting with HoloPy's default package. Even though the accuracy estimates were reasonable for synthetic data, the experimental image quality was heavily polluted by noise sources, such as readout noise, speckle noise, and, due to the size of the weak-phase scatterers and laser power, the shot-noise of the camera. Additionally, the experimental fitting algorithms within HoloPy work by comparing the experiment with other images generated by solving the Lorenz-Mie solutions[33]. Although this could allow for faster convergence, it can also be vulnerable to the aforementioned noise sources. Other fitting algorithms[45] could be used to improve the performance of the fitting scheme. Our proposed interpolant technique, however, was resilient to noise, yielding accurate solutions with high relative precision. This could potentially be explained by the uniform noise distribution in the image. Since the reconstructed peak intensities are the sum of the contributions from the holographic pattern, noisy pixel intensity fluctuations around the mean intensity could be averaged from this operation.

The experimental setup used in this study can be improved considerably for NP detection such as using a higher laser power, a shorter wavelength, a camera with higher quantum efficiency, higher magnification, and more optically smooth micro-channels. However, despite the aforementioned challenges, the proposed technique still accurately measured the particle size and refractive index. It is expected that improvements to the experimental setup would allow the interpolant technique to approach the error found with synthetic data.

The NP samples had to be considerably diluted in our case to provide holograms without caustic interference. Since our method relies on hologram intensity, caustics can cause erroneous reconstructed intensities. Additional algorithms can be explored to reduce this influence and expand the use cases for this technique, such as instant deconvolution, iterative deconvolution, or amplitude and phase retrieval using a Gerchberg-Saxton algorithm[46].

The particles can be differentiated from the background and localized using the intensity value from the scattered field if information from the particle, such as the size and refractive index, is known. Fig. 14 shows an example of using this principle with synthetically generated data, where each particle location was successfully extracted, and differentiated from smaller caustic interference, by thresholding the reconstructed intensity volume with respect to the threshold from the calibration

intensity cube within 10% bounds. This provides a better determination for a threshold intensity value to use when wanting to extract particles within a certain range in poly-disperse samples. However, this hasn't been explored in this work experimentally and is left as a future direction.

5 Conclusions

In this paper, we proposed a new technique using the holographic reconstructed volume intensities acquired from Rayliegh-Sommerfeld back-propagation. An intensity cube was built by simulating holograms of different particle sizes and refractive indices, and retrieving the maximum intensity peak value and location in the reconstructed volume. The particle size was estimated by fitting a Gaussian function at the point of numerical re-focalization, which is defined by the first local minima after the Gouy phase shift. A linear scattered interpolant is constructed from the intensity cube, yielding a function that solves for the refractive index given the other input parameters, namely, the maximum scattered intensity peak location, the peak intensity magnitude, and the particle size. We find that the proposed technique was accurate in estimating and differentiating properties from similarly sized NPs, and that it offered error bounds close to least-squares fitting with synthetic data, a technique that is widely regarded for its accuracy. For experimental data, we find that our technique performed well within the bounds of accuracy for the NPs used and that it offered a considerable improvement to least squares fitting, both when initializing fitting parameters using prior random distributions, and using the values estimated from the technique. Even though the least squares didn't provide accurate results for either case, it is expected that its performance would be improved with higher-quality experimental data or different fitting algorithms. This, however, also proved that our technique was robust, even for noisy data that loses information.

The technique presented has the potential to be used in many areas of particle characterization, such as biologically derived NPs and environmental monitoring. Owing to its fast processing time, and wide-field application, potentially analyzing multiple particles in a reconstructed volume at the same time, this technique could be used for interferometric cytometry applications, counting particles and yielding their concentrations, as well as differentiating between them.

6 CRediT authorship contribution statement

Andres Barrio-Zhang: Conceptualization, Methodology, Software, Formal analysis, Validation, Investigation, Data curation, Visualization, Writing - original draft. **Arezoo M. Ardekani:** Conceptualization, Data curation, Formal analysis, Investigation, Supervision, Project administration, Funding acquisition, Writing - original draft, Writing - review and editing.

7 Acknowledgements

This work was performed under a Project Award Agreement from the National Institute for Innovation in Manufacturing Biopharmaceuticals (NIIMBL) and financial assistance award 70NANB21H085 from the U.S. Department of Commerce, National Institute of Standards and Technology. This work was also supported by National Science Foundation awards CBET-1700961 and CBET-2141404 (to A.M.A.). The authors would like to also acknowledge the financial support from the National Council of Science and Technology (CONACYT) from Mexico.

References

1. Gabor, D. Microscopy by reconstructed wave-fronts. *Proc. Royal Soc. London. Ser. A. Math. Phys. Sci.* **197**, 454–487, DOI: 10.1098/rspa.1949.0075 (1949).

2. Memmolo, P. *et al.* Recent advances in holographic 3D particle tracking. *Adv. Opt. Photonics* **7**, 713, DOI: 10.1364/aop.7.000713 (2015).

3. Tahara, T., Quan, X., Otani, R., Takaki, Y. & Matoba, O. Digital holography and its multidimensional imaging applications: A review. *Microscopy* **67**, 55–67, DOI: 10.1093/jmicro/dfy007 (2018).

4. Cheong, F. C. *et al.* Flow visualization and flow cytometry with holographic video microscopy. *Opt. Express* **17**, 13071, DOI: 10.1364/oe.17.013071 (2009).

5. Shangraw, M. & Ling, H. Improving axial localization of weak phase particles in digital in-line holography. *Appl. Opt.* **60**, 7099, DOI: 10.1364/ao.435021 (2021).

6. Wu, X. *et al.* Holography and micro-holography of particle fields: A numerical standard. *Opt. Commun.* **285**, 3013–3020, DOI: 10.1016/j.optcom.2012.02.101 (2012).

7. Bedrossian, M., El-Kholy, M., Neamati, D. & Nadeau, J. A machine learning algorithm for identifying and tracking bacteria in three dimensions using Digital Holographic Microscopy. *AIMS Biophys.* **5**, 36–49, DOI: 10.3934/biophy.2018.1.36 (2018).

8. Merola, F. *et al.* Tomographic flow cytometry by digital holography. *Light. Sci. Appl.* **6**, 1–7, DOI: 10.1038/lsa.2016.241 (2017).

9. Liebel, M. *et al.* 3D tracking of extracellular vesicles by holographic fluorescence imaging. *Sci. Adv.* **6**, 1–9, DOI: 10.1126/SCIADV.ABC2508 (2020).

10. Zadka, Ł. *et al.* Label-Free Quantitative Phase Imaging Reveals Spatial Heterogeneity of Extracellular Vesicles in Select Colon Disorders. *Am. J. Pathol.* **191**, 2147–2171, DOI: 10.1016/j.ajpath.2021.08.005 (2021).

11. Sanborn, D., He, R., Feng, L. & Hong, J. In situ Biological Particle Analyzer based on Digital Inline Holography. *Biotechnol. Bioeng.* **n/a**, DOI: 10.1002/bit.28338. _eprint: https://onlinelibrary.wiley.com/doi/pdf/10.1002/bit.28338.

12. Min, J. *et al.* Quantitative phase imaging of cells in a flow cytometry arrangement utilizing Michelson interferometer-based off-axis digital holographic microscopy. *J. Biophotonics* **12**, e201900085, DOI: 10.1002/jbio.201900085 (2019). _eprint: https://onlinelibrary.wiley.com/doi/pdf/10.1002/jbio.201900085.

13. Merola, F. *et al.* Tomographic flow cytometry by digital holography. *Light. Sci. & Appl.* **6**, e16241–e16241, DOI: 10.1038/lsa.2016.241 (2017). Number: 4 Publisher: Nature Publishing Group.

14. Sheng, J., Malkiel, E. & Katz, J. Digital holographic microscope for measuring three-dimensional particle distributions and motions. *Appl. Opt.* **45**, 3893–3901, DOI: 10.1364/AO.45.003893 (2006).

15. Cheong, F. C., Krishnatreya, B. J. & Grier, D. G. Strategies for three-dimensional particle tracking with holographic video microscopy. *Opt. Express* **18**, 13563, DOI: 10.1364/oe.18.013563 (2010).

16. Toloui, M. & Hong, J. High fidelity digital inline holographic method for 3D flow measurements. *Opt. Express* **23**, 27159, DOI: 10.1364/oe.23.027159 (2015).

17. Toloui, M., Mallery, K. & Hong, J. Improvements on digital inline holographic PTV for 3D wall-bounded turbulent flow measurements. *Meas. Sci. Technol.* **28**, 044009, DOI: 10.1088/1361-6501/aa5c4d (2017).

18. Cheong, F. C. *et al.* Holographic characterization of colloidal particles in turbid media. *Appl. Phys. Lett.* **111**, 153702, DOI: 10.1063/1.4999101 (2017). Publisher: American Institute of Physics.

19. Wu, X. *et al.* Holography and micro-holography of particle fields: A numerical standard. *Opt. Commun.* **285**, 3013–3020, DOI: 10.1016/j.optcom.2012.02.101 (2012).

20. Fung, J., Perry, R. W., Dimiduk, T. G. & Manoharan, V. N. Imaging multiple colloidal particles by fitting electromagnetic scattering solutions to digital holograms. *J. Quant. Spectrosc. Radiat. Transf.* **113**, 2482–2489, DOI: 10.1016/j.jqsrt.2012.06.007 (2012).

21. Vandewiele, S., Strubbe, F., Schreuer, C., Neyts, K. & Beunis, F. Low coherence digital holography microscopy based on the Lorenz-Mie scattering model. *Opt. Express* **25**, 25853–25866, DOI: 10.1364/OE.25.025853 (2017). Publisher: Optica Publishing Group.

22. Dimiduk, T. G. & Manoharan, V. N. A Bayesian approach to analyzing holograms of colloidal particles. .

23. Hannel, M. D., Abdulali, A., O'Brien, M. & Grier, D. G. Machine-learning techniques for fast and accurate feature localization in holograms of colloidal particles. *Opt. Express* **26**, 15221, DOI: 10.1364/oe.26.015221 (2018). 1804.06885.

24. Shao, S., Li, C. & Hong, J. A hybrid image processing method for measuring 3D bubble distribution using digital inline holography. *Chem. Eng. Sci.* **207**, 929–941, DOI: 10.1016/j.ces.2019.07.009 (2019).

25. Shao, S., Mallery, K. & Hong, J. Machine learning holography for measuring 3D particle distribution. *Chem. Eng. Sci.* **225**, 115830, DOI: 10.1016/j.ces.2020.115830 (2020).

26. Altman, L. E. & Grier, D. G. CATCH: Characterizing and Tracking Colloids Holographically Using Deep Neural Networks. *The J. Phys. Chem. B* acs.jpcb.9b10463, DOI: 10.1021/acs.jpcb.9b10463 (2020).

27. Martin, C. *et al.* In-line holographic microscopy with model-based analysis. *Nat. Rev. Methods Primers* **2** (2022).

28. Wilson, L. & Zhang, R. 3D Localization of weak scatterers in digital holographic microscopy using Rayleigh-Sommerfeld back-propagation. *Opt. Express* **20**, 16735, DOI: 10.1364/oe.20.016735 (2012).

29. Latychevskaia, T. & Fink, H.-W. Holographic time-resolved particle tracking by means of three-dimensional volumetric deconvolution. *Opt. Express* **22**, 20994, DOI: 10.1364/oe.22.020994 (2014).

30. Latychevskaia, T. & Fink, H.-W. Practical algorithms for simulation and reconstruction of digital in-line holograms. *Appl. Opt.* **54**, 2424, DOI: 10.1364/ao.54.002424 (2015). 1412.3674.

31. Dixon, L., Cheong, F. C. & Grier, D. G. Holographic deconvolution microscopy for high-resolution particle tracking. *Opt. Express* **19**, 16410, DOI: 10.1364/OE.19.016410 (2011).

32. Romanov, A. V., Maltsev, V. P. & Yurkin, M. A. Retrieving refractive index of single spheres using the phase spectrum of light-scattering pattern. *Opt. & Laser Technol.* **161**, 109141, DOI: 10.1016/j.optlastec.2023.109141 (2023).

33. Barkley, S. *et al.* Holographic Microscopy with Python and HoloPy. *Comput. Sci. Eng.* **22**, 72–82, DOI: 10.1109/MCSE.2019.2923974 (2020). 1806.00058.

34. Martin, C., Leahy, B. & Manoharan, V. N. Improving holographic particle characterization by modeling spherical aberration. *Opt. Express* **29**, 18212, DOI: 10.1364/OE.424043 (2021).

35. Katz, J. & Sheng, J. Applications of Holography in Fluid Mechanics and Particle Dynamics. *Annu. Rev. Fluid Mech.* **42**, 531–555, DOI: 10.1146/annurev-fluid-121108-145508 (2010). _eprint: https://doi.org/10.1146/annurev-fluid-121108-145508.

36. Darakis, E. *et al.* Processing of digital holograms for size measurements of microparticlese. 715524, DOI: 10.1117/12.814578 (Unknown, Singapore, 2008).

37. Darakis, E. *et al.* Microparticle characterization using digital holography. *Chem. Eng. Sci.* **65**, 1037–1044, DOI: 10.1016/j.ces.2009.09.057 (2010).

38. Tian, L., Loomis, N., Domínguez-Caballero, J. & Barbastathis, G. Quantitative measurement of size and three-dimensional position of fast-moving bubbles in air-water mixture flows using digital holography. *Appl. optics* **49**, 1549–54, DOI: 10.1364/AO.49.001549 (2010).

39. Guildenbecher, D. R., Gao, J., Reu, P. L. & Chen, J. Digital holography simulations and experiments to quantify the accuracy of 3D particle location and 2D sizing using a proposed hybrid method. *Appl. Opt.* **52**, 3790, DOI: 10.1364/AO.52.003790 (2013).

40. Molaei, M., Barry, M., Stocker, R. & Sheng, J. Failed escape: Solid surfaces prevent tumbling of Escherichia coli. *Phys. Rev. Lett.* **113**, 1–6, DOI: 10.1103/PhysRevLett.113.068103 (2014).

41. Kashkanova, A. D. *et al.* Precision single-particle localization using radial variance transform. *Opt. Express* **29**, 11070, DOI: 10.1364/OE.420670 (2021).

42. Hart, S. J. & Terray, A. V. Refractive-index-driven separation of colloidal polymer particles using optical chromatography. *Appl. Phys. Lett.* **83**, 5316–5318, DOI: 10.1063/1.1635984 (2003).

43. H. Miles, R. E., Rudić, S., J. Orr-Ewing, A. & P. Reid, J. Measurements of the wavelength dependent extinction of aerosols by cavity ring down spectroscopy. *Phys. Chem. Chem. Phys.* **12**, 3914–3920, DOI: 10.1039/B923758E (2010). Publisher: Royal Society of Chemistry.

44. van der Pol, E., Coumans, F. A. W., Sturk, A., Nieuwland, R. & van Leeuwen, T. G. Refractive Index Determination of Nanoparticles in Suspension Using Nanoparticle Tracking Analysis. *Nano Lett.* **14**, 6195–6201, DOI: 10.1021/nl503371p (2014).

45. Markwardt, C. B. Non-linear Least Squares Fitting in IDL with MPFIT (2009). ArXiv:0902.2850 [astro-ph].

46. Latychevskaia, T. Three-dimensional volumetric deconvolution in coherent optics and holography. *Appl. Opt.* **60**, 1304, DOI: 10.1364/AO.412736 (2021).